

EXPERIMENTAL AND NUMERICAL INVESTIGATION OF TURBULENT MIXING FIELDS BEHIND BLUFF BODY JETS

Krishna MOHANARANGAM^{1*}, Darrin W. STEPHENS², Xiaodong CAO^{1,4}, Phillip D. FAWELL³, Kosta SIMIC¹ and William YANG¹

¹ CSIRO Mineral Resources, Clayton, Victoria 3169, AUSTRALIA

² Applied CCM Pty Ltd, Dandenong North, Victoria, 3175, AUSTRALIA

³ CSIRO Mineral Resources, Waterford, WA 6152, AUSTRALIA

⁴ Tianjin Key Lab of Indoor Air Environmental Quality Control, School of Environmental Science and Engineering, Tianjin University, Tianjin 300072, CHINA

*Corresponding author, E-mail address: krishna.mohanarangam@csiro.au

ABSTRACT

Bluff body shapes are used to promote better heat and mass transfer in various industrial flow situations, flow past them serving to enhance turbulence and thereby promote mixing, primarily due to the vortex shedding created. In this paper, the turbulent mixing field for flow past a square sparge jet is investigated both experimentally and numerically. The geometry considered for this study is a square channel fitted with a square sparge located midway along its length. Time Resolved – Particle Image Velocimetry (TR-PIV) measurements were conducted to measure and quantify the mixing and the turbulent fields behind the sparge. Measurements were carried out at a frequency of 1 KHz to capture the unsteady behaviour of the flow past the sparge and its jet. Computational Fluid Dynamics (CFD) simulation of the set-up was carried out by solving Unsteady Reynolds Averaged Navier Stokes (URANS) equations with the $k-\omega$ model as turbulence closure. Various ratios between the bulk flow past the sparge and that of its jet were considered to investigate the turbulent behaviour of the sparge geometry, while also providing data for model development and calibration. The long-term aim is to identify sparge designs that provide enhanced mixing in industrial flow settings.

NOMENCLATURE

a_1	SST $k-\omega$ turbulence model constant
d	wall distance
f	body force
F_1	first SST blending function
F_2	second SST blending function
k	turbulence kinetic energy
p'	modified pressure
P_k	shear production of turbulence
R_{ij}	Reynolds stresses
S_{ij}	strain rate tensor
t	time
u	velocity
x	stream-wise direction
y	normal direction
z	span-wise direction
α_ω	SST $k-\omega$ turbulence model constant
β^*	SST $k-\omega$ turbulence model constant

β_ω	SST $k-\omega$ turbulence model constant
ν	kinematic viscosity
ν_t	kinematic turbulent viscosity
σ_k	$k-\omega$ turbulence model constant
σ_ω	SST $k-\omega$ turbulence model constant
ϕ_1	inner model constant
ϕ_2	outer model constant
ω	turbulence frequency

Subscripts

i, j, k	components
mag	magnitude

Superscript

($\bar{\quad}$)	Favre-averaged
-------------------	----------------

INTRODUCTION

Transport and mixing of scalar quantities, such as chemical or thermal fluxes, is central in many engineering and environmental applications. Understanding the turbulent transport of these scalar quantities is necessary to design devices like mixers, reactors and combustion chambers of the highest efficiency and with compliance to stringent emission standards. Confined jets have predominantly been used to transport scalar quantities due to their nature to induce efficient momentum exchange within their surrounding environment (Kandakure *et al.*, 2008; Yule *et al.*, 1993).

In the class of jet flows turbulent mixing of confined co-axial jets is a complex dynamics process which finds applications in a number of engineering devices, such as ejectors, industrial burners, jet engine combustion chambers and after burners. The flow field arising from the interaction of co-axial jets and their mixing behaviour has been shown to comprise of three main zones: i) initial merging zone where the two annular streams enter the mixing duct with their respective axial velocities, ii) intermediate merging zone where the largest momentum exchange between the jets occurs, iii) fully merged zone where flow conditions become progressively similar to a single jet (Ahmed and Sharma, 2000).

The factors that are involved in the mixing process of these jets are also responsible for its complexity. They include: velocity ratio, temperature ratio, density ratio,

compressibility and turbulence levels of the two streams, swirl, pressure gradient, interaction between wall bounded and free shear flows, mixing duct to inner jet nozzle diameter ratio and the thickness of the inner duct wall (Buresti *et al.*, 1994). Of this list, only the last two factors contribute predominantly to how the jet mixing is affected as a function of its shape or design which the current study is aimed to investigate.

In this paper, turbulent mixing of a confined bluff body jet is investigated both experimentally and numerically. The bluff body is a square sparge, centrally located in a square channel flow. Three different velocity ratios between sparge jet and surrounding channel were studied to understand their flow interactions. Physical measurements were conducted using Time Resolved – Particle Image Velocimetry (TR-PIV). Computational Fluid Dynamics (CFD) modelling was carried out by solving Unsteady Reynolds Averaged Navier Stokes (URANS) equations with the $k-\omega$ model as turbulent closure. Good agreement was observed between experimental and numerical findings. The turbulent mixing behaviour within the measurement domain is highly dependent on the jet when the velocity ratio is less than 1. The effect of the jet is observed until the end of the measurement domain.

EXPERIMENTAL SETUP AND CONFIGURATION

Figure 1 shows the set-up and flow loop used in this study. The basic design consists of the square channel flow with a square sparge/bluff body placed perpendicular to the flow. The square channel section of the rig was fitted with square-to-round transition piece at its inlet and outlet ends. Water was re-circulated through the channel using a centrifugal pump (DAVEY ISO[®] spec) that can reach flow rates in excess of $50 \text{ m}^3 \text{ h}^{-1}$ from a 5 m^3 holding tank. The water flow rate in the channel was measured using a 3-inch Danfoss[®] electromagnetic flow meter. Flow to the sparge was provided with the aid of a progressive cavity pump (Mono CP-11 connected). The flow metering for the sparge was done using a Micro Motion[®] Coriolis type mass flow meter.

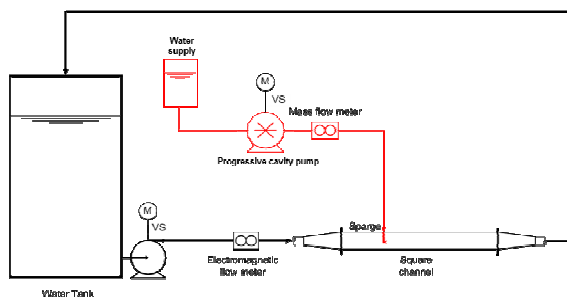


Figure 1: Flow loop used for measurements.

The square channel used in the current study was scaled to $5D$, with D representing the width of the sparge. The sparge was placed centrally inside the square channel as shown in Figure 2. TR-PIV measurements were conducted along the centreline of the square channel geometry as shown in Figure 3.

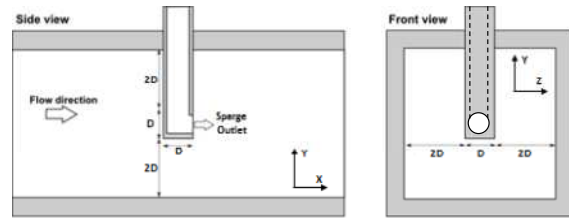


Figure 2: Schematic and dimensions of the square sparge.

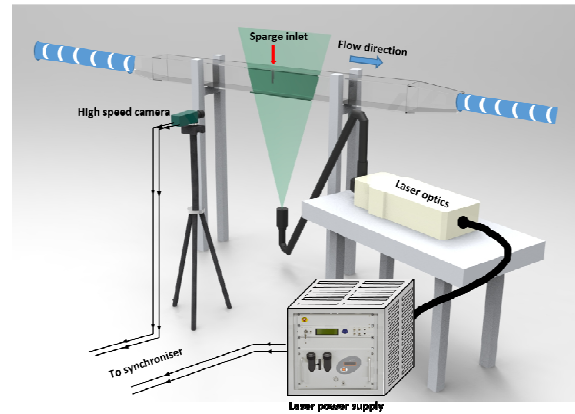


Figure 3: TR-PIV set-up of the experiment.

The TR-PIV system used comprised of a Litron diode pumped, dual cavity Nd:YLF laser system (LDY 304) capable of producing an output energy of 30 mJ at 1 kHz repetition frequency at a wavelength of 527 nm . The system is capable of reaching frequencies up to 10 kHz at reduced output energies. Three different flow velocity ratios between the sparge exit and the channel were studied (0.5 , 1.0 and 2.0). In all three cases studied, the velocity through the sparge was maintained as a constant and the flow through the square channel was modified to achieve the required velocity ratio. The acquisition frequency of the TR-PIV system was set to 1 kHz and a total of 12000 uncorrelated image pairs were acquired in each case to obtain the time-averaged flow quantities. The area of the region of interest was set to $0.270 \times 0.055 \text{ m}^2$.

The analysis of the acquired TR-PIV images was performed using DynamicStudio software version 4.0 (Dantec Dynamics[®]). The background stray image noise was first removed using image background subtraction. The subtracted images were then subjected to a multi-grid adaptive PIV method, with a maximum and a minimum interrogation area of 64×64 pixels and 32×32 pixels, respectively, and a grid step size of 8×8 pixels. The adaptive PIV method iteratively optimizes the size and shape of each interrogation area using the prescribed step size to adapt to local flow gradients and seeding densities, finally leading to a spatial resolution of $1.8 \times 1.8 \text{ mm}^2$. Peak validation combined with a local neighbourhood validation was used to eliminate spurious velocity vectors resulting from local insufficient seeding or background noise. The bad correlations would be rejected when the ratio between the first and second highest correlation peak in an interrogation window was less than 1.3 . Therefore, there was a significant correlation peak to accurately estimate the velocity vector in each interrogation window. Further information on the image techniques can be obtained from the DynamicStudio user guide.

MODEL DESCRIPTION

The CFD model was based on the incompressible Unsteady Reynolds Averaged Navier-Stokes (URANS) equations:

Continuity Equation:

$$\partial_i u_i = 0 \quad (1)$$

Momentum Equation:

$$\partial_i u_i + u_j \partial_j u_i = -\partial_i p' + \nu \partial_{ii} u_i - \partial_j \overline{R_{ij}} + f_i \quad (2)$$

where u_i is the fluid velocity, p' the modified pressure, ν the kinematic viscosity, $\overline{R_{ij}} = \overline{u_i u_j}$ the Reynolds stresses and f_i is the body force.

The k - ω SST (Shear Stress Transport) two-equation model uses the gradient hypothesis to relate the Reynolds stresses to the mean velocity gradients and the turbulent viscosity.

$$-\overline{R_{ij}} = \nu_t (\partial_i \overline{u_j} + \partial_j \overline{u_i}) \quad (3)$$

The turbulent viscosity is defined as the product of a turbulent velocity and the turbulent length scale. In two-equation models, the turbulence velocity scale is computed from the turbulence kinetic energy (k) solution of a transport equation. The turbulent length scale is estimated from the turbulence kinetic energy and its frequency (ω).

The transport equations for k and ω are given by equations (4) and (5), respectively (Menter et al., 2003):

$$\partial_i k + u_j \partial_j k = \partial_j ((\nu + \sigma_k \nu_t) \partial_j k) + \min(P_k, 10\beta^* k \omega) - \beta^* k \omega, \quad (4)$$

$$\partial_i \omega + u_j \partial_j \omega = \partial_j ((\nu + \sigma_\omega \nu_t) \partial_j \omega) + \alpha_\omega \frac{\omega}{k} \min(P_k, 10\beta^* k \omega) - \beta_\omega \omega^2 + 2(1 - F_1) \frac{\sigma_{\omega_2}}{\omega} \partial_j k \partial_j \omega. \quad (5)$$

The k - ω model does not account for the transport of the turbulent shear stress, which results in an over-prediction of eddy-viscosity, and ultimately leads to a failure in predicting the onset and amount of flow separation from smooth surfaces. The proper transport behaviour can be obtained by using a limiter in the formulation of the eddy-viscosity and is given by:

$$\nu_t = \frac{a_1 k}{\max(a_1 \omega, \mathbf{S}_{mag} F_2)}, \quad (6)$$

where

$$\mathbf{S}_{mag} = \sqrt{2S_{ij} S_{ij}}. \quad (7)$$

Each constant is a blend of an inner and outer constant, via

$$\phi = F_1 \phi_1 + (1 - F_1) \phi_2 \quad (8)$$

where ϕ_1 represents the inner constant and ϕ_2 the outer constant. The blending function F_1 is given by:

$$F_1 = \tanh(\arg_1^4), \quad (9)$$

with additional functions given by:

$$\arg_1 = \min \left[\max \left(\frac{\sqrt{k}}{\beta^* \omega d}, \frac{500\nu}{d^2 \omega} \right), \frac{4\sigma_{\omega_2}}{CD_{k\omega} d^2} \right], \quad (10)$$

$$CD_{k\omega} = \max \left(\frac{2\sigma_{\omega_2}}{\omega} \partial_j k \partial_j \omega, 10^{-10} \right). \quad (11)$$

The second blending function, F_2 , is given by:

$$F_2 = \tanh(\arg_2^2), \quad (12)$$

with

$$\arg_2 = \max \left(\frac{2\sqrt{k}}{\beta^* \omega d}, \frac{500\nu}{d^2 \omega} \right). \quad (13)$$

The model constants are $\beta^* = 0.09$ and $a_1 = 0.31$, with the remaining values shown in Table 1.

Table 1: SST model constants.

	α_ω	σ_k	σ_ω	β
ϕ_1	0.5556	0.85	0.5	0.075
ϕ_2	0.44	1.0	0.856	0.0828

Numerical Method

The conservation equations of mass, momentum and turbulence given above were solved using a finite volume method to determine the liquid velocity for comparison against the experimental data. A hybrid computational grid consisting of 888,155 elements arranged to achieve good cell quality (see Figure 4) was used. At the inlets, a uniform velocity with turbulence quantities calculated from mixing length theory is applied. A Neumann condition was applied to all flow quantities at the channel outlet. Zero velocity is assumed on all walls where an adaptive wall function is used.

A transient solver implemented in OpenFOAM version 2.2.2 was used. Pressure-velocity coupling was achieved via the PISO algorithm (Issa, 1985). For the discretisation of time-dependent terms, the 1st order Euler scheme was used. Pressure and velocity gradients were calculated by the Green-Gauss method. A 2nd order linear upwind discretisation scheme was used for the advection terms. A steady-state solution using the k - ω SST turbulence model was applied to initialise each of the transient simulations. A time-step that gave a maximum Courant number of two (giving a mean ~ 0.05) was used for the simulations. The procedure for each simulation was to run for an initial time of ~ 15 residence times, followed by a further 75 residence times where the simulations data were time averaged. The initial time period was determined to be sufficient for the flow to develop. Time averaging over the remaining time appeared to be sufficient duration for statistical sampling of mean quantities. All simulations were conducted on a HPC cluster utilising 60 Intel Xeon E5-2620v3 cores per simulation. Infiniband was used for communication between the cluster compute nodes.

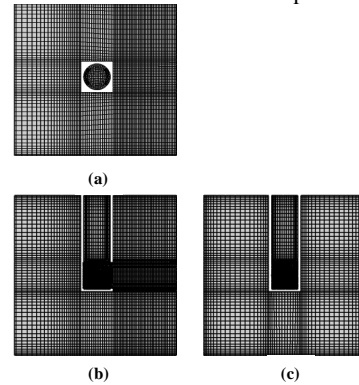


Figure 4: Zoomed section of the channel showing the mesh around and inside the sparge (a) plan view, (b) side view and (c) end view.

RESULTS

Figure 5 shows the streamline plot generated from the experimental mean velocities of the flow past the sparge at three different velocity ratios. As PIV measurements capture the whole 2-dimensional flow field at an instant in time, streamline plots provide a comparison of major flow features behind the sparge. A re-circulation region is found behind the sparge across all the velocity ratios opposite to the general flow direction. The centre or the eye of the recirculation vortex is found to vary with the on-coming channel flow velocities. There is also the presence of a small counter-rotating re-circulation region on the top of the larger region close to the top wall of the channel flow. This region is more prominent at the lower channel flow velocity, which gives rise to a complex three-dimensional flow pattern above the sparge exit.

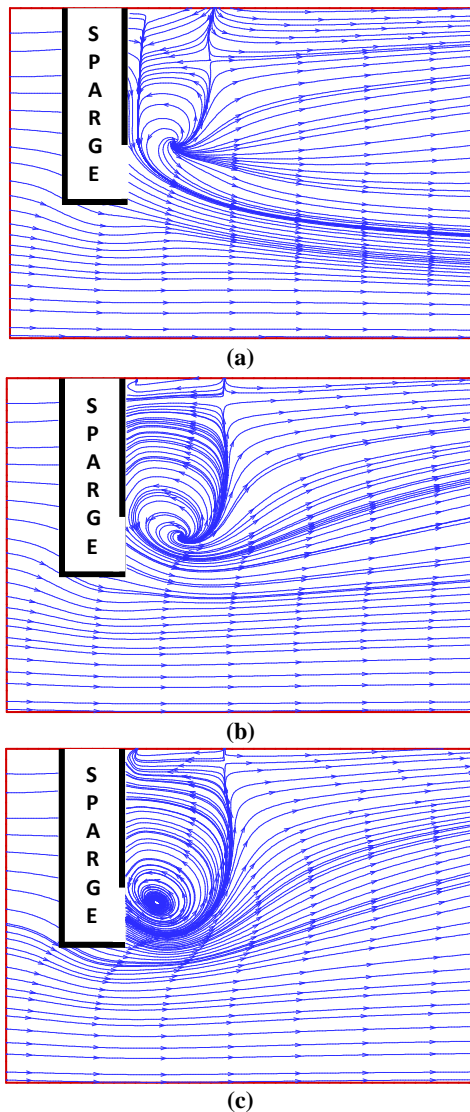


Figure 5: Streamline plot (experimental) of flow behind the sparge at 0.5 (a), 1.0 (b) and 2.0 (c) velocity ratios.

The flow leaving the sparge has a downward momentum close to its exit, which is shown prominently at the lower channel flow velocity. This downward momentum exerted by the flow exiting the sparge is dissipated with an increase in oncoming channel flow velocity.

Figure 6 shows the comparison of simulated data (solid lines) against experimental results (symbols) for mean stream-wise velocities (flow direction) behind the sparge exit. The horizontal axis depicts the velocities normalised against their respective oncoming channel flow velocities and the vertical axis shows the normalised channel height. The jet emanating from the sparge is clearly visible for the lower velocity ratio case. The simulated results, whilst not able to accurately capture the sparge jet velocity, show a good overall agreement with measured data above and below the sparge exit. Under-prediction of the simulated result is seen until 10 diameters downstream of the sparge exit.

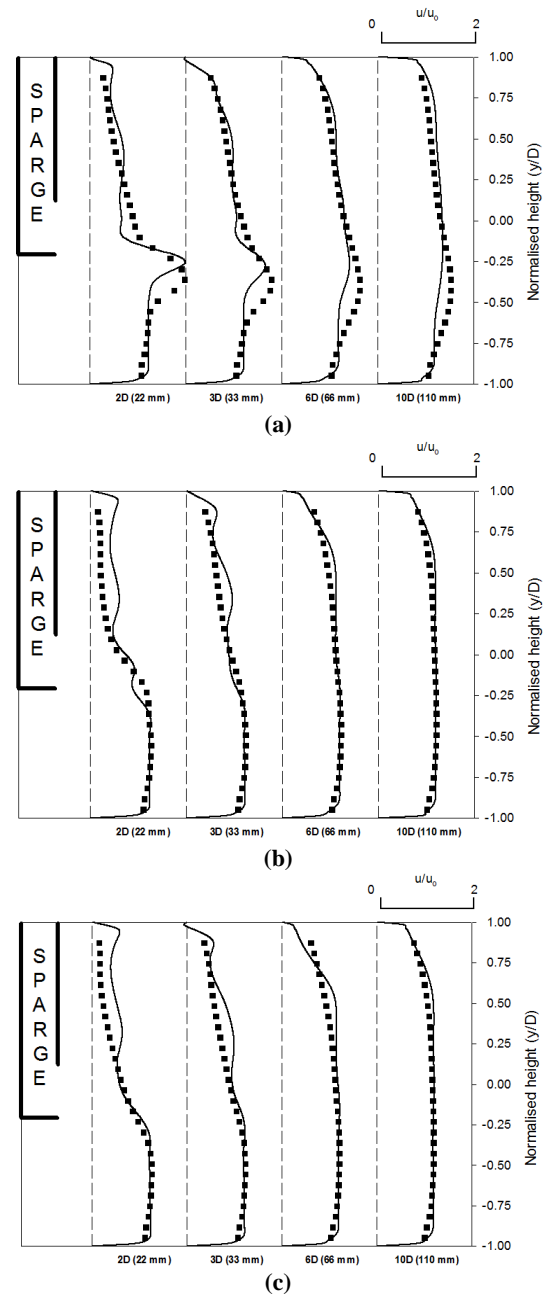


Figure 6: Comparison of experimental (symbols) and simulated (lines) mean stream-wise flow velocities behind the sparge at 0.5 (a), 1.0 (b) and 2.0 (c) velocity ratios.

The mean velocities for the other two velocity ratios (1.0 and 2.0) show almost a similar trend between them. There is a drop in the mean velocity magnitude above the exit of

the sparge for both these cases. The simulated velocities show minor over-predictions close to and above the sparge exit. However, as the flow assumes a developed channel flow profile (i.e. several diameters downstream of the sparge) the simulated velocities compare well with the experimental measurements.

Figure 7 shows the simulated streamline plot of the flow past the sparge as seen from the top across the XZ plane on the mid-section of the sparge outlet or half-way through the channel section. Measurements were not carried out using TR-PIV across this plane during this experimental campaign. The results were plotted using the averaged velocities that were used to compare the simulation results with experimental measurements.

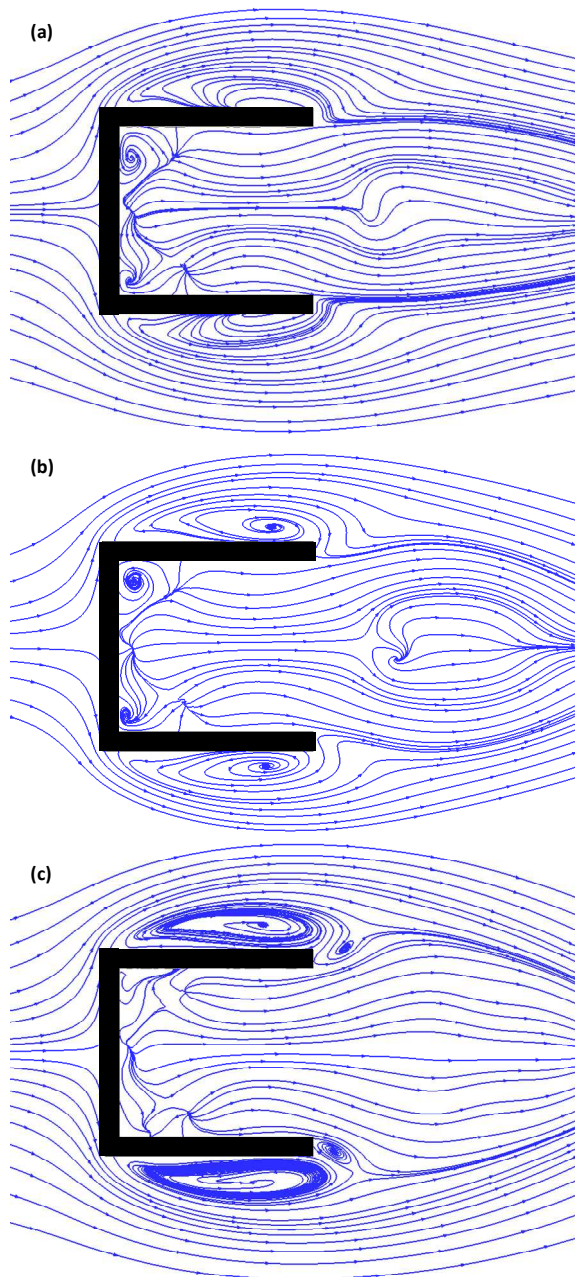


Figure 7: Streamline plot (simulated) of flow behind the sparge at 0.5 (a), 1.0 (b) and 2.0 (c) velocity ratios.

The streamline flow patterns show distinctive behaviour across the three different velocity ratios. As flow impinges on the (outside) side wall of the sparge they split and move along the top and bottom of the sparge wall(s). The emergence of recirculating flow patterns are seen on both the top and bottom walls for the lowest flow velocity ratio. This pattern becomes more pronounced with the increase in channel flow velocity, with two distinctive recirculation regions or vortices on the top and bottom walls of the sparge. The momentum energy of the oncoming channel flow sets up these re-circulation patterns wherein part of the energy is stored (and eventually dissipated) in the form of a vortex, as predicted by the simulations. This would also aid to explain the prominence of this pattern with the subsequent increase in channel flow velocity. In fact, it can be seen that there is a creation of additional small vortices at the front edges of the top and bottom walls of the sparge for the highest flow velocity.

The flow pattern inside the sparge shows the presence of two counter-rotating vortices close to the inside top and bottom walls of the sparge. Their presence is prominent in the lower and similar velocity ratio cases, but distinctively absent in the highest flow velocity case. Instead, a complex three-dimensional flow pattern is seen. From the results it can be stated that the increased channel flow velocity has an effect on the flow pattern inside the sparge in the form of back pressure.

To obtain a better understanding of the interaction of bluff body jets with the oncoming flow, the mean stream-wise centreline velocity along the sparge exit (and the channel geometry) is plotted in Figure 8. The vertical axis shows mean velocities normalised against the channel flow velocities while the horizontal axis shows the distance downstream of the sparge. The simulated results (lines) are plotted along with the experimental measurements (symbols). The mean velocities close to the sparge show a drop ($< 2D$) before recovering to match (and exceed) the oncoming channel flow velocities. The drop in mean velocity (in spite of the presence of the jet outlet) is primarily due to the development of a wake region behind the sparge geometry while the increase in centre-line velocity beyond the channel flow velocity is caused by the combined action of the jet emanating from the sparge and the oncoming flow behind it.

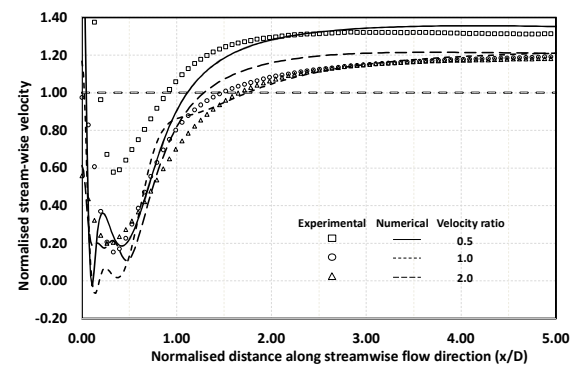


Figure 8: Stream-wise velocities of flow behind the sparge at 0.5 (a), 1.0 (b) and 2.0 (c) velocity ratios along the stream-wise (x) direction.

Unlike a free shear turbulent jet (Hussein *et al.*, 1994), which does not take into account the shape of the sparge or the freestream flow across it, the bluff body jets investigated in this study exhibit a drop in mean velocities in proximity to the jet while further downstream they show an increase in the normalised velocities exceeding the oncoming channel flow velocities. Future work will also investigate the presence of any self-similarity behaviour within these bluff body jets inherently present in free shear turbulent jets.

The lower velocity ratio case is also seen to recover quicker to match the freestream channel flow velocity compared to the other two cases, with the drop in mean velocity more pronounced for higher velocity ratios (compared to 0.5). The presence of the jet downstream of the flow is more pronounced for the lower velocity ratio case, with the normalised velocities on average 10-20% higher than the similar and higher velocity ratio along the centreline.

In the region very close to the sparge exit, i.e., $\leq 0.5D$, velocity peaks could be found across various velocity ratio cases with the peak more pronounced for the lowest velocity ratio. This feature is more clearly seen with the simulated results as the measurements using the current set-up do not have the resolution to resolve these features. The simulated results show the most discrepancy to the measurements for the lower velocity ratio case both before and after the mean velocity recovery regions. There is also an over-prediction of mean velocities for the highest velocity ratio case after the recovery.

Figure 9 shows the simulated mean stream-wise velocities across the span-wise (z) direction of the geometry along the mid-plane (Figure 7) at a distance of $2D$ from the sparge exit. The drop in velocities below the mean channel flow velocities (< 1) increase with an increase in velocity ratios (1.0 and 2.0). However, the lowest velocity ratio case (0.5) shows an increase in mean velocity close to the walls of the sparge (> 1.25) before experiencing a drop. The increased velocity regions close to the sparge walls will also give rise to a region of high shear which could aid in providing better mixing. The magnitude of the velocity drop for this case is half-way between the other two velocity ratios considered in the study.

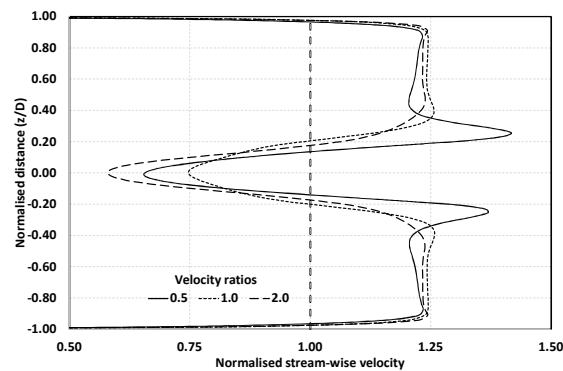


Figure 9: Stream-wise velocity (simulated) of flow behind the sparge at 0.5 (a), 1.0 (b) and 2.0 (c) velocity ratios along the span-wise (z) direction.

Figure 10 shows the Turbulence Kinetic Energy (TKE) plots comparing the measured and simulated data across the various velocity ratios considered. The simulated data is seen to over-predict the values in close proximity to the jet at locations $2D$ and $3D$. Further downstream, the TKE values drop where the comparison between the simulation and measurement is good. It should be noted that the TKE values generated for the lowest velocity ratio are several times higher than those for the higher velocity ratios when normalised against their channel flow velocities.

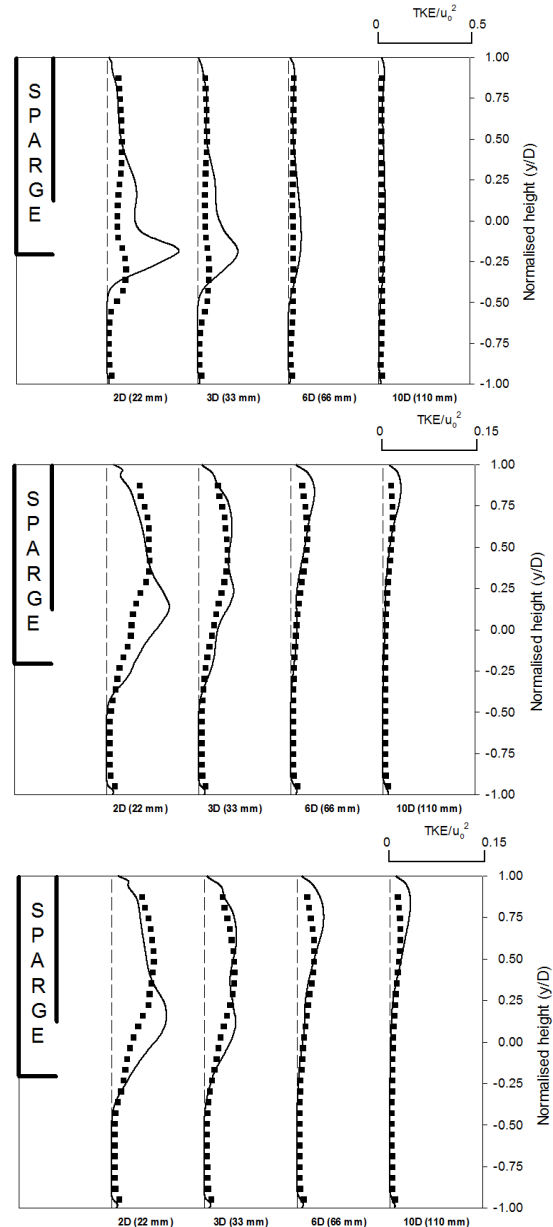


Figure 10: Comparison of experimental (symbols) and simulated (lines) TKE plots of flow behind the sparge at 0.5 (a), 1.0 (b) and 2.0 (c) velocity ratios.

In an attempt to better understand the coherent flow structures that could be present within the flow field and their formation mechanisms, the measured Reynolds stresses from TR-PIV measurements are analysed further. Reynolds stress signifies the turbulent transport of the momentum term and plays a pivotal role in turbulence

production, making it an important parameter for URANS modelling conducted in this work. Physically, Reynolds stress is defined as the vertical flux of the horizontal momentum at a point produced by opposing velocity fluctuations within a flow field. Measured Reynolds stress can be decomposed into four quadrants as defined by the signs of u' and v' , i.e. stream-wise and normal fluctuating velocities, respectively, as shown in Figure 11.

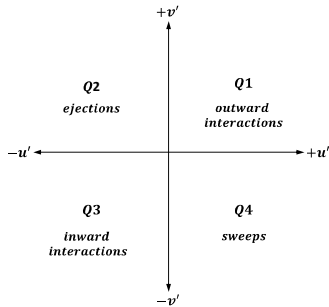


Figure 11: Reynolds stress decomposition.

Values in quadrant 1 (Q1) occur when $u' > 0$ and $v' > 0$; values in this quadrant are responsible for outward interactions of the turbulent structure formed within the flow field. Q2, when $u' < 0$ and $v' > 0$, leads to the ejection or burst events. Q3, when $u' < 0$ and $v' < 0$, leads to the inward interactions, while Q4, when $u' > 0$ and $v' < 0$, leads to sweep events. By definition, both ejections and sweeps contribute positively to Reynolds stress generation. Ejections result from fluid moving away from the jet via motions with faster than average vertical velocity and slower than average stream-wise velocity, while sweeps result from an inrush of fluid with faster than average stream-wise velocity and slower than average vertical motion (Lu and Willmarth, 1973; Jackson, 1976).

Figure 12 shows the Reynolds stress normalised against their respective channel flow (squared) velocities. Discrepancies between measurement and simulations are seen close to the sparge exit. The measurement setup with the current field of view is not setup to resolve flow features very close to the sparge. There are some similarities between measured and simulated results in the bulk of the region away from the sparge exit. The lowest velocity ratio shows a significant presence of ejection and sweep phenomenon within the measured domain, i.e. $\overline{u'v'} < 0$, compared to the other two ratios considered. Ejection and sweep events are the main turbulence energy producers and their presence is important for mixing. The measured data will be analysed further to see whether the ejection or the sweep phenomena have the most dominant role at this velocity ratio. Across all the ratios, the Q1 and Q3 events leading to outward and inward interactions, respectively, show a significant presence within the measured flow field.

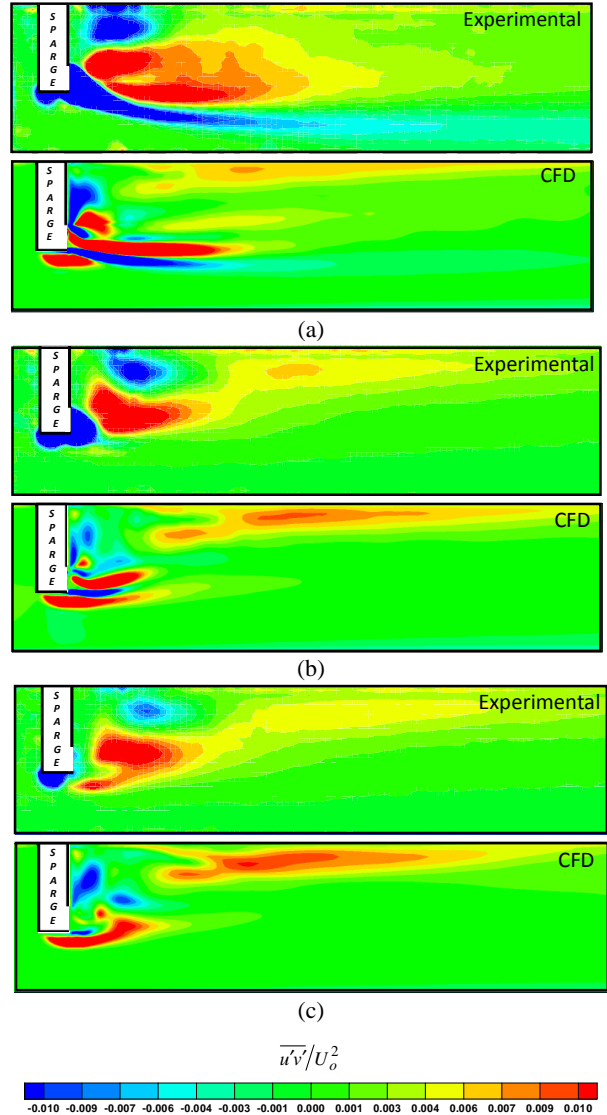


Figure 12: Reynolds stress contour plot for velocity ratios of 0.5 (a), 1.0 (b) and 2.0 (c).

CONCLUSION

Experimental and numerical modelling of flow past a bluff body jet was studied. The square sparge with a round outlet was located inside a square channel. The velocity ratios between the outer channel and the sparge were varied (0.5, 1.0 and 2.0) to study the effect of velocity ratios on the sparge jet. Time Resolved-Particle Image Velocimetry (TR-PIV) was used in the experimental investigation, while Unsteady Reynolds Averaged Navier-Stokes (URANS) was used for numerical simulation. The simulated mean velocities compare well with the measured averaged flow velocities. The simulated TKE close to the jet region consistently over-predicts the measured data while showing good comparisons further downstream. Reynolds stress decomposition of the jet flow across various velocity ratios show that ‘ejection’ and ‘sweep’ events, which are main contributors to the turbulence kinetic energy, are predominant at the lowest velocity ratio while ‘inward’ and ‘outward’ interactions show significant presence at velocity ratios of 1.0 and 2.0.

REFERENCES

- AHMED, M. R. and SHARMA, S. D. (2000), "Effect of velocity ratio on the turbulent mixing of confined, co-axial jets", *Exp. Therm. Fluid Sci.*, 22, 19-33.
- BURESTI, G., TALAMELLI, A. and PETAGNA, P. (1994). "Experimental characterization of the velocity field of a coaxial jet configuration" *Exp. Thermal Fluid Sci.*, 9, 135-146.
- HUSSIEN, J. H., CAPP, S. P. and GEORGE, W. K. (1994). "Velocity Measurements in a High Reynolds Number Momentum Conserving, Axisymmetric, Turbulent Jet", *J. Fluid Mechanics*, 258, 31-75.
- ISSA, R. (1985). "Solution of the implicitly discretised fluid flow equations by operator splitting", *J. Comp. Phys.*, 61, 40.
- JACKSON, R. G. (1976). "Sedimentological and fluid-dynamic implications of the turbulent bursting phenomenon in geophysical flows", *J. Fluid Mechanics*, 77, 531-560.
- KANDAKURE, M.T., PATKAR, V.C., and PATWARDHAN, A.W. (2008). "Characteristics of turbulent confined jets", *Chemical Engineering and Processing: Process Intensification*, 47, 1234-1245.
- LU, S. S. and WILLMARTH, W. W. (1973). "Measurements of the structure of the Reynolds stress in a turbulent boundary layer", *J. Fluid Mechanics*, 60, 481-511.
- MENTER, F.R., KUNTZ, M., and LANGTRY, R. (2003). "Ten years of industrial experience with the SST turbulence models", *Turbulence, Heat and Mass Transfer 4*, Begell House Inc., 625-632.
- YULE, A.J., DAMOU, M., and KOSTOPOULOS, D. (1993). "Modelling confined jet flow", *Int. J. of Heat and Fluid Flow*, 14, 10-17.